symmetry

IMPACT FACTOR 2.2

CITESCORE 5.4

Article

A Study of the Neutron Skin of Nuclei with Dileptons in Nuclear Collisions

Ke Xu and Baoyi Chen

Special Issue
Symmetry/Asymmetry in Quantum Mechanics

Edited by
Dr. Baoyi Chen

MDPI

https://doi.org/10.3390/sym16091195

symmetry

MDPI

Article

A Study of the Neutron Skin of Nuclei with Dileptons in Nuclear Collisions

Ke Xu [1] and Baoyi Chen [2,*]

[1] Phillips Academy Andover, 180 Main Street, Andover, MA 01810, USA
[2] Department of Physics, Tianjin University, Tianjin 300354, China
* Correspondence: baoyi.chen@tju.edu.cn

Abstract: We studied the photoproduction of dileptons from strong electromagnetic fields generated by the nucleus in relativistic heavy-ion collisions. The production of dileptons is calculated based on the Equivalent Photon Approximation (EPA) method, which depends on the strength of the electromagnetic fields and the density of protons in the nucleus. With the EPA method, we construct the connections between dilepton photoproduction and the electromagnetic form factors in the nucleus. Finally, the nuclear proton densities can be determined with the dilepton photoproduction, which is employed to extract the neutron skin in the nucleus. Our calculations indicate that the dilepton photoproduction varies evidently with different proton densities in the nucleus, suggesting a deeper symmetry underlying the connections between proton density (or the neutron skin) and the dilepton photoproduction. This offers a new way to study the neutron skin in the nucleus.

Keywords: relativistic heavy-ion collisions; photoproduction; dilepton; neutron skin; equivalent photon approximation

Citation: Xu, K.; Chen, B. A Study of the Neutron Skin of Nuclei with Dileptons in Nuclear Collisions. *Symmetry* **2024**, *16*, 1195. https://doi.org/10.3390/sym16091195

Academic Editor: Manuel Gadella

Received: 25 July 2024
Revised: 1 September 2024
Accepted: 6 September 2024
Published: 11 September 2024

1. Introduction

In relativistic heavy-ion collisions, a new form of deconfined nuclear matter composed of quarks and gluons is expected to emerge in the early stages [1]. This quark–gluon plasma (QGP) resembles the state of the early universe shortly after the Big Bang. Identifying signals and studying the properties of this deconfined matter have become crucial topics in high-energy physics [2,3]. At the Relativistic Heavy-Ion Collider (RHIC) and the Large Hadron Collider (LHC), nuclear matter undergoes a crossover phase transition [4–7], with a violent expansion. Heavy quarkonium, produced in initial parton hard scatterings, experiences dissociation in the QGP. The thermal partons with color charges can reduce the binding energies of quarkonium, a phenomenon known as the color screening effect. Additionally, inelastic scatterings of partons can lead to the dissociation of quarkonium bound states. These processes result in the suppression of heavy quarkonium yields, which can serve as a signal of the hot, deconfined matter in heavy-ion collisions [8–11]. Light hadrons are also used to probe the properties of this deconfined matter. The observed quark-number-scaling behavior in the collective flows of light hadrons [12] suggests that the hot medium is predominantly composed of light quarks rather than hadrons during the violent expansion. Moreover, the large collective flows are well described by hydrodynamic models [13,14]. The deconfined medium is found to behave as a nearly perfect fluid with low viscosity [15,16].

When nuclei are accelerated to nearly the speed of light, strong electromagnetic fields are generated by the protons [17–21]. In the direction of nuclear motion, these electromagnetic fields undergo Lorentz contraction. The transverse electromagnetic fields can reach $eB \sim 5m_\pi^2$ in Au+Au collisions at the RHIC ($\sqrt{s_{NN}} = 200$ GeV) [22], and approximately $\sim 70m_\pi^2$ in semi-central Pb+Pb collisions at the LHC [18]. These strong electromagnetic fields influence the motion of light quarks and induce phenomena such as the Chiral

Magnetic Effect [23], the Chiral Vortical Effect [24], and Magnetic Catalysis [25,26]. Additionally, the elliptic flows of charged particles are modified by in-medium electromagnetic fields [27,28]. Heavy quarks and quarkonia are also affected by these strong electromagnetic fields [29–31]. Magnetic fields can induce direct flows in D mesons [32] and charmonium [33], and they can generate spin polarization of light hadrons [34] and heavy quarks [35] in relativistic heavy-ion collisions.

Electromagnetic fields can also produce vector mesons [36] or dileptons [37–39], a process known as photoproduction. This mechanism is predominant in ultra-peripheral nuclear collisions, where hadronic interactions are negligible [40–43]. To study photoproduction, electromagnetic fields can be quantized as quasi-real photons using Equivalent Photon Approximation (EPA) [44], a method further extended by Weizsäcker and Williams [45]. The energy density of these photons is derived from the energy density of electromagnetic fields. In coherent photoproduction, the wavelength of the equivalent photon exceeds the nuclear radius, resulting in photon interactions with the entire nucleus [46–48]. Consequently, the typical transverse momentum of photoproduced vector mesons can be estimated as $p_T \sim 1/R_A$, where R_A is the nuclear radius. Conversely, in incoherent photoproduction, where the wavelength of the equivalent photon is short enough to resolve individual nucleons, the process is termed incoherent photoproduction [49,50]. In this regime, photoproduced vector mesons typically exhibit very low transverse momentum. Photoproduction remains observable in peripheral collisions at RHIC [51] and LHC [52] energies.

Photoproduction serves as a sensitive probe for assessing both the strength of these fields and the proton distribution within the nucleus. In heavy nuclei, some neutrons may reside on the surface, forming a neutron skin. The neutron skin can be quantified as the difference between the root mean square (RMS) radii of protons and neutron distributions, with experimental evidence supporting its existence [53]. The neutron skin is related to proton density and photoproduction of dileptons.

This paper is organized as follows. Section 2 outlines the proton and neutron distributions within Pb nuclei, along with the corresponding form factor calculations used for quasi-real photon calculations. Section 3 gives the densities of photons. In Section 4, we compute the photoproduction of dileptons in ultra-peripheral and peripheral collisions. Finally, Section 5 provides a summary.

2. Nuclear Structure

The nucleus comprises protons and neutrons. Recent studies indicate that these particles may not be uniformly distributed within the nucleus. Specifically, a neutron skin covers the nucleus, while protons, carrying positive charges, are distributed internally. To investigate the electric charge distribution, we propose calculating the photoproduction of dileptons, which can be measured in experiments [54–56]. Assuming isotropic densities of protons and neutrons within the nucleus, the spatial distribution of nucleons has been effectively parameterized using the Woods–Saxon distribution [57], as follows:

$$\rho(r) = \frac{\rho_0}{1+\exp(\frac{r-r_0}{a})}, \quad (1)$$

where $r_0 = 6.624$ fm represents the Pb nuclear radius. $a = 0.549$ fm describes the edge of the nucleus. ρ_0 is the normalization factor ensuring $\int d\mathbf{r}\,\rho(r) = A$. For the Pb nucleus, we adopt $\rho_0 = 0.1604/A$ fm^{-3} with $A = 208$. To determine the neutron skin and proton density within the nucleus, we assume that both proton and neutron densities follow the Woods–Saxon distribution, but with different parameter values. Specifically, we consider two types of proton densities based on the Woods–Saxon distribution. One set of parameters is $r_0 = 6.624$ fm and $a = 0.549$ fm, while the other corresponds to $r_0 = 6.924$ fm and

$a = 0.549$ fm. Using these proton densities, one can calculate the root-mean-square radii of protons and neutrons, $R_i = \sqrt{\langle r^2 \rangle}$, as follows:

$$\langle r^2 \rangle = \int \rho(r) r^2 d^3 r \Big/ \int \rho(r) d^3 r. \tag{2}$$

where $\rho(r)$ represents the distribution of either protons or neutrons. When the densities of protons and neutrons are the same, the value of R_p and R_n are 5.74 fm, calculated with the first kind of proton density. The neutron skin of the nucleus is expected to be around 0.2 fm. Therefore, the parameters of the second proton density are taken to be $R_p = 5.52$ fm. The two types of proton densities and the neutron density are depicted in Figure 1. In the scenario without a neutron skin, where protons and neutrons are uniformly distributed within the nucleus, the root-mean-square radius of protons (and neutrons) is $R_p = 5.74$ fm, as shown in Figure 1.

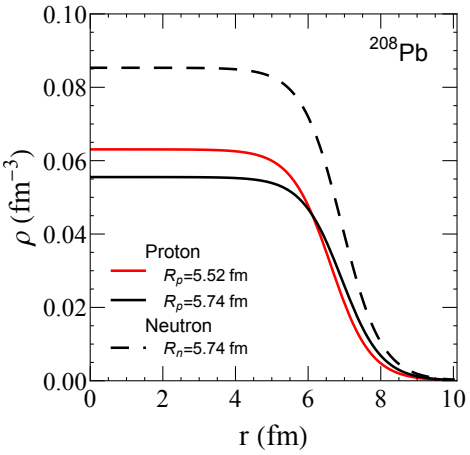

Figure 1. The densities of the protons and the neutrons in the nucleus *Pb*. When without the neutron skin, the root-mean-square radii of the proton and neutron distributions are the same, $R_p = 5.74$ and $R_n = 5.74$. If a neutron skin is introduced, the value of R_p is $R_p = 5.52$ fm.

After considering different distributions for the protons and neutrons, the difference between R_p and R_n, referred to as the neutron skin R_{skin}, is defined as

$$R_{skin} \equiv R_n - R_p. \tag{3}$$

We will employ two different proton density distributions to calculate dilepton photoproduction in relativistic heavy-ion collisions. Given that dilepton photoproduction is sensitive to proton densities within the nucleus, it can serve to quantify the neutron skin. To compute dilepton photoproduction arising from the interaction of two transverse electromagnetic fields generated by two nuclei, we approximate these electromagnetic fields as swarms of quasi-real photons. The strength of these fields correlates with the densities of these quasi-real photons, which depend on the electromagnetic form factors. The form factor $F(q)$ is connected with the charge distribution via the Fourier transformation, as follows:

$$F(\vec{q}) = \int \rho^{norm}(r) e^{i\vec{q}\cdot\vec{r}} d^3\vec{r}. \tag{4}$$

where $\rho(r)$ represents the proton densities normalized by the atomic mass number A. Averaging over angles yields the form factor $F(q) = \frac{1}{4\pi} \int \sin(\theta)\, d\theta\, d\phi\, F(\vec{q})$, as depicted in Figure 2. With normalized proton densities, the form factor approaches unity as q approaches 0. The magnitude of the form factor varies with q due to the Fourier transformation and the finite volume of electric charge densities. There is an oscillation and

decrease in the $|F(q)|$ in Figure 2. The behavior of the oscillation comes from the integration of an exponential function in Equation (4), which can be regarded as a sum of sin and cos functions with different weights $\rho^{\text{norm}}(r)$. If the charge density is a delta function, then $|F(q)| = 1$ is uniform at all q. On the other hand, if the protons are uniformly distributed over an extremely large volume, then the form factor $|F(q)|$ approaches a delta function located at q=0. Therefore, the form factor $|F(q)|$ at a large q value corresponds to the charge distribution $\rho(r)$ at a small r value. In Figure 2, the two form factors significantly differ at a large q value. This discrepancy arises because the two proton densities differ notably at a small r value. However, despite the substantial difference in the form factors of the two proton densities at a large q value, the dilepton photoproduction calculated using these densities shows a smaller difference. This is because photoproduction is determined by integrating the form factors over the entire q range. Consequently, the neutron skin has a less pronounced effect on the mass spectrum of dilepton photoproduction compared to the form factor.

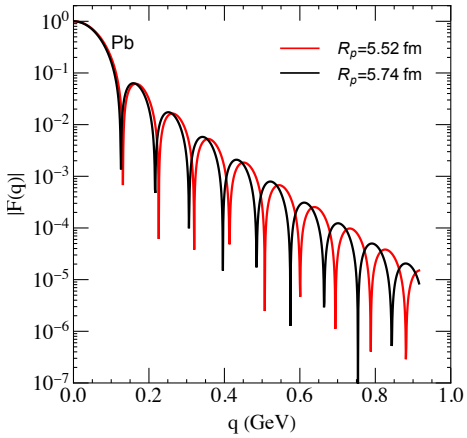

Figure 2. The form factors of the nucleus Pb as a function of the momentum q. Two kinds of proton distributions are taken to calculate the form factors. The radii characterizing the proton distribution are taken as $R_p = 5.52$ fm and 5.74 fm, respectively).

3. Quasi-Real Photon Density

In relativistic heavy-ion collisions, the electromagnetic fields generated by the moving nucleus are Lorentz-contracted in the longitudinal direction, defined as the nuclear moving direction. These transverse electromagnetic fields can be quantized as photons. The spatial and energy density of photons is determined by the energy flux of the electromagnetic fields. EPA methods have derived the formula of photon density, which depends on the electromagnetic form factor $F(q)$. Therefore, in the transverse plane, the photon density at the position $\vec{x}_T$ is [37,54]

$$n(\omega, \vec{x}_\perp) = \frac{4Z^2\alpha}{\omega}\left|\int \frac{d^2k_\perp}{(2\pi)^2} k_\perp \frac{F(\sqrt{k_\perp^2 + \omega^2/\gamma_L^2})}{k_\perp^2 + \omega^2/\gamma_L^2} e^{i\vec{x}_\perp \cdot \vec{k}_\perp}\right|^2, \quad (5)$$

where $\alpha = 1/137$ is the fine structure constant. Photon transverse momentum and energy are denoted as $\vec{k}_T$ and w, respectively. As there is a significant Lorentz contraction in the electromagnetic fields, this effect is considered with the Lorentz factor $\gamma_L = \sqrt{s_{NN}}/(2m_N)$ in the formula, where m_N is the mass of protons. As $F(q)$ represents the form factor of normalized electric charge density, the square of the electric charges or the protons Z^2 is multiplied in the photon density.

The photon densities as a function of distance are depicted in Figure 3. Different lines correspond to two kinds of proton densities, as previously described. A noticeable distinc-

tion between the two types of photon densities is evident within the nuclear radius range. As photon energy increases, the photon density decreases. Consequently, photoproduction significantly diminishes in regions of larger transverse momentum where particles are generated by high-energy photons.

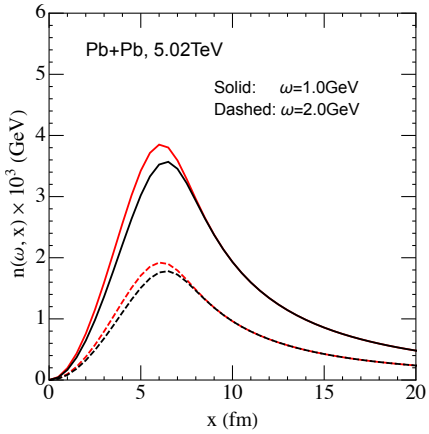

Figure 3. The densities of quasi-real photons as a function of the distance x in Pb+Pb collisions at the energy $\sqrt{s_{NN}} = 5.02$ TeV. Solid and dashed lines represent the photon spatial distribution with the energy $w = 1$ and 2 GeV, respectively. Red and black lines correspond to the case with the root-mean-square radius of the proton distribution of $R_p = 5.52$ and 5.74 fm, respectively.

4. Photoproduction

In the framework of the Equivalent Photon Approximation, dileptons arise from collisions involving two quasi-real photons emitted by two nuclei [58]. The distribution of photoproduced dileptons is connected with photon energy densities and proton distributions. Consequently, dilepton photoproduction, measurable in experiments, serves as a way to investigate the strength of electromagnetic fields and the proton density within the nucleus, which finally helps to constrain the neutron skin of the nucleus. The energy densities of photons were computed in previous sections. To describe the photoproduced dilepton, we introduce the invariant mass M of a dilepton and rapidity y. Their connections with the energies of two photons (w_1, w_2) are

$$M = \sqrt{4\omega_1\omega_2}, \tag{6}$$

$$y = \frac{1}{2}\ln(\frac{\omega_1}{\omega_2}). \tag{7}$$

The production probability of dileptons depends on a two-photon scattering cross-section and two-photon densities. It is written as a function of the invariant mass M and rapidity y of dilepton pair, as follows:

$$P(M,y,b) = \frac{M}{2}\int d^2r n_1(\omega_1, r_{1\perp}) n_2(\omega_2, r_{2\perp}) \times \sigma(\gamma\gamma \to l^+l^-), \tag{8}$$

where $r_{1\perp} = \sqrt{r^2 + b^2/4 - br\cos(\theta)}$ and $r_{2\perp} = \sqrt{r^2 + b^2/4 + br\cos(\theta)}$ are the distance between the scattering position of two photons and the center of nuclei 1 and 2, respectively. b is the impact parameter of two colliding nuclei. $n_i(\omega_i, r_i)$ is the photon density given by Equation (5). The dilepton production cross-section in the reaction $\gamma + \gamma \to l^+ + l^-$ is given by the Breit–Wheeler formula [59],

$$\sigma(\gamma\gamma \to l^+l^-) = \frac{4\pi\alpha^2}{M^2}[(2 + \frac{8m^2}{M^2} - \frac{16m^4}{M^4}) \times \ln(\frac{M + \sqrt{M^2 - 4m^2}}{2m}) - \sqrt{1 - \frac{4m^2}{M^2}}(1 + \frac{4m^2}{M^2})]. \quad (9)$$

By utilizing the photon–photon scattering cross-section and approximating photon densities that reflect the strength of electromagnetic fields, one can compute the production of dileptons via photoproduction. In ultra-peripheral collisions, these calculations are straightforward, as there are no hadronic collisions; instead, the entire nucleus contributes to the electromagnetic fields and subsequent photoproduction. Conversely, for impact parameters $b < 2R_A$, hadronic collisions occur within the overlapping region of two nuclei. Nucleons involved in these collisions do not generate significant electromagnetic fields nor contribute to photoproduction. This distinction is crucial in semi-central heavy-ion collisions. To address this, we introduce the probability of hadronic collisions $P_H(b)$.

$$P_H(b) = 1 - \exp\left[-\sigma_{NN}^{inel} \int d\mathbf{r} T_A(\mathbf{r} - \frac{\mathbf{b}}{2}) T_B(\mathbf{r} + \frac{\mathbf{b}}{2})\right], \quad (10)$$

where σ_{NN}^{inel} denotes the inelastic cross-sections of nucleon–nucleon collisions, $T_{A/B}$ represents the nuclear thickness function of nuclei A and B, defined as the integration of the nucleon density over the longitudinal direction, $T_i(\mathbf{r}) = \int \rho(\mathbf{r}_\perp, z)\, dz$, where ρ denotes the nucleon distribution. The probability $P_H(b)$ approaches zero at ultra-peripheral collisions.

The photoproduction of dileptons can be suppressed by hadronic collisions. These collisions diminish the intensity of electromagnetic fields and reduce the density of quasi-real photons. Accounting for this adjustment, dilepton photoproduction $\frac{d^2N_{l^+l^-}}{dMdy}$ in peripheral and semi-central collisions with fixed centrality is accordingly corrected as $\frac{d^2N_{l^+l^-}}{dMdy} = \int_{b_{min}}^{b_{max}} dbP(W, y, b)P_H(b) / \int_{b_{min}}^{b_{max}} dbP_H(b)$ [60], where the impact parameters $b_{\min}$ and $b_{\max}$ represent the minimum and maximum values in a specific collision centrality. The differential mass spectrum of dielectrons, $d^2N/dMdy$, in $\sqrt{s_{NN}} = 5.02$ TeV Pb+Pb collisions is illustrated in Figure 4. Photoproduction is computed for different collision centralities: 0–10%, 20–40%, and 30–50%. Two different proton density distributions are utilized to calculate electromagnetic form factors and photon densities in photoproduction. The discrepancy between these two scenarios is approximately 10% in central collisions, reducing in more peripheral collisions due to the similar electromagnetic fields further from the nucleus under the differing proton distributions. This inspires us to determine the proton density and neutron skin through dilepton photoproduction in low invariant mass regions. Note that experimental data were obtained before regarding dilepton production in ultra-peripheral heavy-ion collisions and peripheral hadronic collisions at RHIC Au+Au [61] and LHC Pb+Pb [62] collisions. Theoretical studies on dielectron photoproduction in peripheral collisions are also available in [63,64], where the invariant mass spectrum of dielectrons has been calculated. To effectively compare our calculations with experimental data, particularly for dielectrons in peripheral and semi-central collisions, it is essential to account for additional contributions from the quark–gluon plasma (QGP) in dilepton production. This aspect will be addressed in our future work.

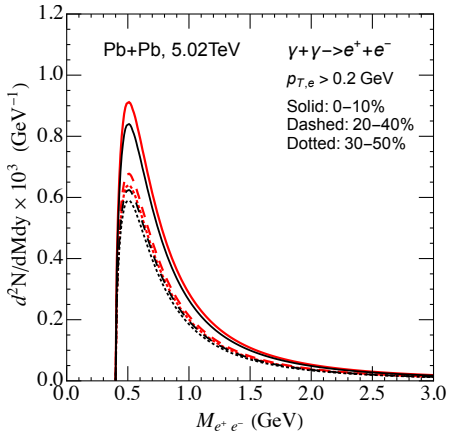

Figure 4. The differential dielectron mass spectrum $d^2N/dMdy$ in $\sqrt{s_{NN}} = 5.02$ TeV Pb+Pb collisions with different centrality bins. The red lines correspond to the proton distribution with $R_p = 5.52$ fm, while the black lines correspond to the proton distribution with $R_p = 5.74$ fm.

5. Summary

In summary, strong electromagnetic fields can induce the photoproduction of vector mesons and dileptons in relativistic heavy-ion collisions.Electromagnetic fields can be approximated by quasi-real photons based on the Equivalent Photon Approximation method. The final invariant mass distribution of dileptons depends on the electromagnetic form factors of the nucleus and photon densities, which carry the information of the proton distribution in the nucleus. This study connects dielectron photoproduction with varying proton densities in the nucleus, which can help extract the neutron skin of the nucleus. Our findings demonstrate a direct relationship between the neutron skin of the nucleus and the yield of photoproduced dielectrons. The dependence of dielectron photoproduction on proton density is sensitive in semi-central collisions but still evident in ultra-peripheral collisions (UPCs), offering a novel approach to quantifying the neutron skin of the nucleus.

Author Contributions: Methodology, K.X.; formal analysis, K.X.; formal analysis, K.X.; investigation, K.X. and B.C.; writing—review and editing, K.X. and B.C.; supervision, B.C.; funding acuisition, B.C.; All authors have read and agreed to the published version of the manuscript.

Funding: This work was supported by the National Natural Science Foundation of China (NSFC) under Grant No. 12175165.

Data Availability Statement: The original contributions presented in the study are included in the article, further inquiries can be directed to the corresponding authors.

Conflicts of Interest: The authors declear no conflicts of interest.

References

1. Bazavov, A.; Bhattacharya, T.; Cheng, M.; DeTar, C.; Ding, H.T.; Gottlieb, S.; Gupta, R.; Hegde, P.; Heller, U.M.; Karsch, F.; et al. The chiral and deconfinement aspects of the QCD transition. *Phys. Rev. D* **2012**, *85*, 054503. [CrossRef]
2. Gazdzicki, M.; Gorenstein, M.; Seyboth, P. Onset of deconfinement in nucleus-nucleus collisions: Review for pedestrians and experts. *Acta Phys. Polon. B* **2011**, *42*, 307–351. [CrossRef]
3. Adams, J. et al. [STAR]. Experimental and theoretical challenges in the search for the quark gluon plasma: The STAR Collaboration's critical assessment of the evidence from RHIC collisions. *Nucl. Phys. A* **2005**, *757*, 102–183. [CrossRef]
4. Stephanov, M.A. QCD phase diagram: An Overview. *PoS LAT* **2006**, *2006*, 024.
5. Luo, X.; Shi, S.; Xu, N.; Zhang, Y. A Study of the Properties of the QCD Phase Diagram in High-Energy Nuclear Collisions. *Particles* **2020**, *3*, 278–307. [CrossRef]
6. Huang, M.; Zhuang, P. QCD Matter and Phase Transitions under Extreme Conditions. *Symmetry* **2023**, *15*, 541. [CrossRef]
7. Rougemont, R.; Grefa, J.; Hippert, M.; Noronha, J.; Noronha-Hostler, J.; Portillo, I.; Ratti, C. Hot QCD phase diagram from holographic Einstein–Maxwell–Dilaton models. *Prog. Part. Nucl. Phys.* **2024**, *135*, 104093. [CrossRef]
8. Matsui, T.; Satz, H. J/ψ Suppression by Quark-Gluon Plasma Formation. *Phys. Lett. B* **1986**, *178*, 416–422. [CrossRef]

9. Liu, Y.; Chen, B.; Xu, N.; Zhuang, P. Y Production as a Probe for Early State Dynamics in High Energy Nuclear Collisions at RHIC. *Phys. Lett. B* **2011**, *697*, 32–36. [CrossRef]
10. Zhao, X.; Rapp, R. Medium Modifications and Production of Charmonia at LHC. *Nucl. Phys. A* **2011**, *859*, 114–125 [CrossRef]
11. Yao, X.; Müller, B. Quarkonium inside the quark-gluon plasma: Diffusion, dissociation, recombination, and energy loss. *Phys. Rev. D* **2019**, *100*, 014008. [CrossRef]
12. Adare, A. et al. [PHENIX]. Scaling properties of azimuthal anisotropy in Au+Au and Cu+Cu collisions at s(NN) = 200-GeV. *Phys. Rev. Lett.***2007**, *98*, 162301. [CrossRef] [PubMed]
13. Song, H.; Heinz, U.W. Causal viscous hydrodynamics in 2+1 dimensions for relativistic heavy-ion collisions. *Phys. Rev. C* **2008**, *77*, 064901. [CrossRef]
14. Schenke, B.; Jeon, S.; Gale, C. Elliptic and triangular flow in event-by-event (3+1)D viscous hydrodynamics. *Phys. Rev. Lett.* **2011**, *106*, 042301. [CrossRef]
15. Liu, S.Y.F.; Rapp, R. *T*-matrix Approach to Quark-Gluon Plasma. *Phys. Rev. C* **2018**, *97*, 034918. [CrossRef]
16. He, M.; van Hees, H.; Rapp, R. Heavy-quark diffusion in the quark–gluon plasma. *Prog. Part. Nucl. Phys.* **2023**, *130*, 104020. [CrossRef]
17. Skokov, V.; Illarionov, A.Y.; Toneev, V. Estimate of the magnetic field strength in heavy-ion collisions. *Int. J. Mod. Phys. A* **2009**, *24*, 5925–5932. [CrossRef]
18. Deng, W.T.; Huang, X.G. Event-by-event generation of electromagnetic fields in heavy-ion collisions. *Phys. Rev. C* **2012**, *85*, 044907. [CrossRef]
19. Voronyuk, V.; Toneev, V.D.; Cassing, W.; Bratkovskaya, E.L.; Konchakovski, V.P.; Voloshin, S.A. (Electro-)Magnetic field evolution in relativistic heavy-ion collisions. *Phys. Rev. C* **2011**, *83*, 054911. [CrossRef]
20. Tuchin, K. Particle production in strong electromagnetic fields in relativistic heavy-ion collisions. *Adv. High Energy Phys.* **2013**, *2013*, 490495. [CrossRef]
21. Wang, Z.; Zhao, J.; Greiner, C.; Xu, Z.; Zhuang, P. Incomplete electromagnetic response of hot QCD matter. *Phys. Rev. C* **2022**, *105*, L041901. [CrossRef]
22. Huang, X.G. Electromagnetic fields and anomalous transports in heavy-ion collisions—A pedagogical review. *Rept. Prog. Phys.* **2016**, *79*, 076302. [CrossRef] [PubMed]
23. Fukushima, K.; Kharzeev, D.E.; Warringa, H.J. The Chiral Magnetic Effect. *Phys. Rev. D* **2008**, *78*, 074033. [CrossRef]
24. Jiang, Y.; Huang, X.G.; Liao, J. Chiral vortical wave and induced flavor charge transport in a rotating quark-gluon plasma. *Phys. Rev. D* **2015**, *92*, 071501. [CrossRef]
25. Shovkovy, I.A. Magnetic Catalysis: A Review. *Lect. Notes Phys.* **2013**, *871*, 13.
26. Bruckmann, F.; Endrodi, G.; Kovacs, T.G. Inverse magnetic catalysis and the Polyakov loop. *JHEP* **2013**, *1304*, 112. [CrossRef]
27. Tuchin, K. On viscous flow and azimuthal anisotropy of quark-gluon plasma in strong magnetic field. *J. Phys. G* **2012**, *39*, 025010. [CrossRef]
28. Basar, G.; Kharzeev, D.; Skokov, V. Conformal anomaly as a source of soft photons in heavy ion collisions. *Phys. Rev. Lett.* **2012**, *109*, 202303. [CrossRef]
29. Alford, J.; Strickland, M. Charmonia and Bottomonia in a Magnetic Field. *Phys. Rev. D* **2013**, *88*, 105017. [CrossRef]
30. Das, S.K.; Plumari, S.; Chatterjee, S.; Alam, J.; Scardina, F.; Greco, V. Directed Flow of Charm Quarks as a Witness of the Initial Strong Magnetic Field in Ultra-Relativistic Heavy Ion Collisions. *Phys. Lett. B* **2017**, *768*, 260. [CrossRef]
31. Zhao, J.; Zhou, K.; Chen, S.; Zhuang, P. Heavy flavors under extreme conditions in high energy nuclear collisions. *Prog. Part. Nucl. Phys.* **2020**, *114*, 103801. [CrossRef]
32. Chatterjee, S.; Zek, P.B. Large directed flow of open charm mesons probes the three dimensional distribution of matter in heavy ion collisions. *Phys. Rev. Lett.* **2018**, *120*, 192301. [CrossRef] [PubMed]
33. Chen, B.; Hu, M.; Zhang, H.; Zhao, J. Probe the tilted Quark-Gluon Plasma with charmonium directed flow. *Phys. Lett. B* **2020**, *802*, 135271. [CrossRef]
34. Becattini, F.; Karpenko, I.; Lisa, M.; Upsal, I.; Voloshin, S. Global hyperon polarization at local thermodynamic equilibrium with vorticity, magnetic field and feed-down. *Phys. Rev. C* **2017**, *95*, 054902. [CrossRef]
35. Liu, Z.; Bai, Y.; Zheng, S.; Huang, A.; Chen, B. Exploring Spin Polarization of Heavy Quarks in Magnetic Fields and Hot Medium. *arXiv* **2024**, arXiv:2404.02032.
36. Shi, W.; Zha, W.; Chen, B. Charmonium Coherent Photoproduction and Hadroproduction with Effects of Quark Gluon Plasma. *Phys. Lett. B* **2018**, *777*, 399–405. [CrossRef]
37. Krauss, F.; Greiner, M.; Soff, G. Photon and gluon induced processes in relativistic heavy ion collisions. *Prog. Part. Nucl. Phys.* **1997**, *39*, 503. [CrossRef]
38. Klein, S.; Nystrand, J. Exclusive vector meson production in relativistic heavy ion collisions. *Phys. Rev. C* **1999**, *60*, 014903. [CrossRef]
39. Li, G.; Zhou, K.; Chen, B. Effects of nuclear charge fluctuations on dilepton photoproduction. *Commun. Theor. Phys.* **2020**, *72*, 025301. [CrossRef]
40. Bertulani, C.A.; Baur, G. Electromagnetic Processes in Relativistic Heavy Ion Collisions. *Phys. Rept.* **1988**, *163*, 299. [CrossRef]
41. Bertulani, C.A.; Klein, S.R.; Nystrand, J. Physics of ultra-peripheral nuclear collisions. *Ann. Rev. Nucl. Part. Sci.* **2005**, *55*, 271. [CrossRef]

42. Adam, J. et al. [ALICE Collaboration]. Coherent ψ(2S) photo-production in ultra-peripheral Pb Pb collisions at $\sqrt{s_{\mathrm{NN}}}$ = 2.76 TeV. *Phys. Lett. B* **2015**, *751*, 358. [CrossRef]
43. Abelev, B.B. et al. [ALICE Collaboration]. Exclusive J/ψ photoproduction off protons in ultra-peripheral p-Pb collisions at $\sqrt{s_{\mathrm{NN}}}$ = 5.02 TeV. *Phys. Rev. Lett.* **2014**, *113*, 232504. [CrossRef]
44. Fermi, E. On the Theory of the impact between atoms and electrically charged particles. *Z. Phys.* **1924**, *29*, 315. [CrossRef]
45. von Weizsacker, C.F. Radiation emitted in collisions of very fast electrons. *Z. Phys.* **1934**, *88*, 612.
46. Yu, G.; Cai, Y.; Fu, Y.; Yang, H.; Gao, Q.; Hu, Q.; Hu, L.; Li, W.; Song, Y. Coherent Photoproduction of Low-pT Charmonium in Peripheral Heavy Ion Collisions within the Color Dipole Model. *Adv. High Energy Phys.* **2022**, *2022*, 1561632. [CrossRef]
47. Lappi, T.; Mantysaari, H. *J/|psi* production in ultraperipheral Pb+Pb and *p*+Pb collisions at energies available at the CERN Large Hadron Collider. *Phys. Rev. C* **2013**, *87*, 032201. [CrossRef]
48. Zha, W.; Ruan, L.; Tang, Z.; Xu, Z.; Yang, S. Coherent photo-produced J/ψ and dielectron yields in isobaric collisions. *Phys. Lett. B* **2019**, *789*, 238–242. [CrossRef]
49. Yu, G.M.; Cai, Y.B.; Li, Y.D.; Wang, J.S. Heavy quarkonium photoproduction in ultrarelativistic heavy ion collisions. *Phys. Rev. C* **2017**, *95*, 014905. [CrossRef]
50. Yang, Y.; Cai, S.; Cai, Y.; Xiang, W.; Inclusive diffractive heavy quarkonium photoproduction in pp , pA and AA collisions. *Nucl. Phys. A* **2019**, *990*, 17–28. [CrossRef]
51. Adam, J. et al. [STAR Collaboration]. Observation of excess J/ψ yield at very low transverse momenta in Au+Au collisions at $\sqrt{s_{\mathrm{NN}}}$ = 200 GeV and U+U collisions at $\sqrt{s_{\mathrm{NN}}}$ = 193 GeV. *arXiv* **2019**, arXiv:1904.11658.
52. Adam, J. et al. [ALICE Collaboration]. Measurement of an excess in the yield of J/ψ at very low p_{T} in Pb-Pb collisions at $\sqrt{s_{\mathrm{NN}}}$ = 2.76 TeV. *Phys. Rev. Lett.* **2016**, *116*, 222301. [CrossRef]
53. Angeli, I.; Marinova, K.P. Table of experimental nuclear ground state charge radii: An update. *Atom. Data Nucl. Data Tabl.* **2013**, *99*, 69–95. [CrossRef]
54. Zha, W.; Ruan, L.; Tang, Z.; Xu, Z.; Yang, S. Double-slit experiment at fermi scale: coherent photoproduction in heavy-ion collisions. *Phys. Rev. C* **2019**, *99*, 061901. [CrossRef]
55. Luo, J.; Li, X.; Tang, Z.; Wu, X.; Zha, W. Effect of initial nuclear deformation on dielectron photoproduction in hadronic heavy-ion collisions. *Phys. Rev. C* **2023**, *108*, 054906. [CrossRef]
56. Adam, J. et al. [STAR]. Measurement of e^+e^- Momentum and Angular Distributions from Linearly Polarized Photon Collisions. *Phys. Rev. Lett.* **2021**, *127*, 052302. [CrossRef]
57. Jia, J. Shape of atomic nuclei in heavy ion collisions. *Phys. Rev. C* **2022**, *105*, 014905. [CrossRef]
58. Klein, S.R. Two-photon production of dilepton pairs in peripheral heavy ion collisions. *Phys. Rev. C* **2018**, *97*, 054903. [CrossRef]
59. Brodsky, S.J.; Kinoshita, T.; Terazawa, H. Two Photon Mechanism of Particle Production by High-Energy Colliding Beams. *Phys. Rev. D* **1971**, *4*, 1532–1557. [CrossRef]
60. Zha, W.; Klein, S.R.; Ma, R.; Ruan, L.; Todoroki, T.; Tang, Z.; Xu, Z.; Yang, C.; Yang, Q.; Yang, S. Coherent J/ψ photoproduction in hadronic heavy-ion collisions. *Phys. Rev. C* **2018**, *97*, 044910. [CrossRef]
61. Adam, J. et al. [STAR]. Low-p_T e^+e^- pair production in Au+Au collisions at $\sqrt{s_{NN}}$ = 200 GeV and U+U collisions at $\sqrt{s_{NN}}$ = 193 GeV at STAR. *Phys. Rev. Lett.* **2018**, *121*, 132301. [CrossRef] [PubMed]
62. Acharya, S. et al. [ALICE]. Dielectron production at midrapidity at low transverse momentum in peripheral and semi-peripheral Pb–Pb collisions at $\sqrt{s_{\mathrm{NN}}}$ = 5.02 TeV. *JHEP* **2023**, *6*, 24.
63. Yu, K.; Peng, J.; Li, S.; Wu, K.; Xie, W.; Sun, F. Lepton pair photoproduction in hadronic heavy-ion collisions with nuclear overlap. *Phys. Rev. C* **2024**, *109*, 064907. [CrossRef]
64. Wang, R.J.; Lin, S.; Pu, S.; Zhang, Y.F.; Wang, Q. Lepton pair photoproduction in peripheral relativistic heavy-ion collisions. *Phys. Rev. D* **2022**, *106*, 034025. [CrossRef]